


Stability of topologically protected edge states in nonlinear fiber loops

A. Bisianov, M. Wimmer, U. Peschel, and O. A. Egorov

Institute of Solid State Theory and Optics, Friedrich Schiller University Jena, Max-Wien-Platz 1, 07743 Jena, Germany

 (Received 26 August 2019; published 18 December 2019)

We study both theoretically and experimentally the existence and stability of symmetry-protected topological chiral edge states in an all-photon system mimicking Floquet dynamics of a discrete one-dimensional quantum walk in the presence of Kerr nonlinearity. The system is realized via time multiplexing as two fiber loops of slightly different lengths with a dynamically variable coupling strength. We prove that topological edge states persist in the nonlinear regime for moderate intensities, despite chiral symmetry breaking. Above a certain power threshold, they undergo destabilization, resulting in the radiation into the bulk modes. Finally, we show that the nonlinear interaction with bulk modes can serve as an effective pumping of the topological edge states.

DOI: [10.1103/PhysRevA.100.063830](https://doi.org/10.1103/PhysRevA.100.063830)

I. INTRODUCTION

Topological edge and interface states have attracted attention as robust, scattering-free, and efficient transport channels. Originally discovered within condensed-matter physics [1–3], they were later found in various experimentally accessible optical systems: photonic arrays and crystals [4–7], metamaterials [8], coupled resonator arrays [9,10], quasicrystals [11–13], and photonic quantum walks [14]. Furthermore, the realization of topological phases and edge states has been proposed in nonunitary systems [15–17]. A topological protection in the presence of nonlinearity as well as of gain and loss is a new research direction that is very promising for the realization of novel types of devices such as topological insulator lasers [18,19]. Lasing in the topological edge states of one-dimensional (1D) [20] and two-dimensional [21] lattices has been demonstrated under incoherent excitation of microstructured semiconductor microcavities operating in the strong-coupling regime.

In general, the presence of topological phases is predetermined by the underlying symmetries [22–24]. One of them, the so-called chiral symmetry, is responsible for the appearance of topological edge states in the middle of a band gap (zero-energy states) and protects them from all perturbations. The simplest topological system that supports chiral zero-energy edge states is the celebrated Su-Schrieffer-Heeger (SSH) model [25,26], originally introduced to describe the dynamics of noninteracting spinless electrons in a 1D dimer chain. The so-called principle of bulk-boundary correspondence states that the existence of the topological edge states in the lattice is predetermined by the topological invariant of the bulk, which in the case of the SSH model is known as the winding number. An extension of the SSH model to its periodically driven (Floquet) counterpart has been discovered [27,28] and experimentally implemented in photonic quantum walks [14].

In contrast to the noninteracting model, many-body bosonic [29] or fermionic [30] interactions can break chiral symmetry and hence lift the degeneracy of the zero-energy edge state by splitting it into particle and hole counterparts,

which may finally become unstable. Nevertheless, the topologically protected edge states are able to persist even in an open dissipative strongly nonlinear environment, such as exciton-polariton SSH chains fabricated in the appropriately structured semiconductor microcavities [20] or in arrays of coupled split-ring resonators with a magnetic dipole resonance in the GHz frequency range [31]. Strong enhancement of a third-harmonic signal at a topological edge state of a zigzag array of dielectric nanoresonators has been reported [32]. Moreover, the gap solitons forming in the topological gap of 1D bosonic dimer chains [33] demonstrate a chiral behavior. Finally, third-order Kerr nonlinearity can form a self-recovering topological midgap soliton at the edge, even if the SSH lattice is initially in the trivial phase [34]. All this evidence suggest that even if the chiral symmetry is broken in the strict sense, a certain locally defined chiral symmetry still allows topological states to form and persist even in the nonlinear environments.

In this work, we study experimentally and theoretically the interplay between topology and nonlinearity by using an all-photon Floquet-like analog of the SSH lattices (see Fig. 1). Discretization is realized via the time-multiplexing technique with two fiber loops of slightly different lengths that are mutually coupled with a dynamically variable strength. In particular, we focus on the existence and stability of the topologically nontrivial edge state and investigate its robustness with respect to collisions with nonlinear waves. It is worth mentioning that the setup considered here has been established as a versatile and a very coherent platform for discrete light walks and has allowed the study of many fundamental phenomena, such as PT symmetry [35], Berry phase [36], trivial defect states [37], and PT-symmetric solitons [38].

II. THE EXPERIMENTAL PLATFORM AND THE MODEL

The experimental platform comprises two coupled fiber loops having an average length of $\bar{L} \approx 4000$ meters and a mutual length difference of $\Delta L \approx 40$ meters. A pulse of a duration of 25 ns with a carrier wavelength of about 1552 nm is launched into one of the loops. It travels through the

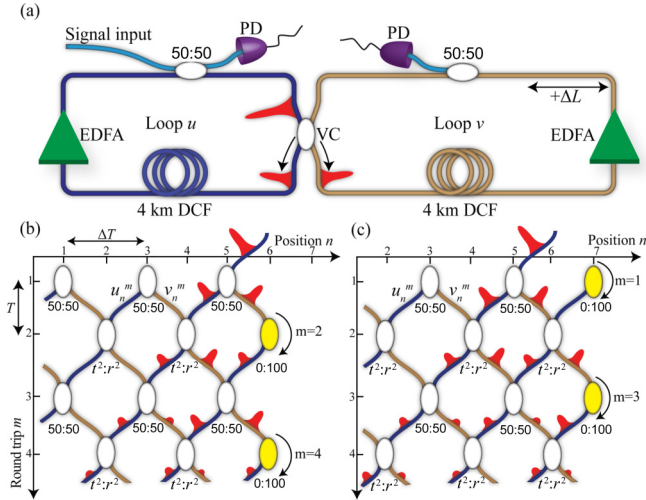


FIG. 1. (a) A basic scheme of the experimental setup comprises two fiber loops of slightly different length ΔL coupled via a voltage-driven fast variable coupler (VC). Pulse injection and extraction is realized via two passive beam splitters. The pulse dynamics is captured via two photodiodes (PDs), one for each loop. The nonlinear self-phase modulation and the energy-loss compensation are ensured by the 4-km-long dispersion-compensating fibers (DCFs) and the erbium-doped fiber amplifiers (EDFAs), respectively. The variable coupler allows one to realize the Floquet analog of the SSH model by alternating its coupling ratio (r^2/t^2) every roundtrip m as well as to introduce a reflecting boundary in the position space n . (b),(c) The pulse dynamics in the fiber loops mapped onto a 1+1D lattice, where one roundtrip in the short loop u_n^m (blue color) stands for the motion from northeast to southwest, while the propagation from northwest to southeast is equivalent to one roundtrip through the long loop v_n^m (brown-golden color). The reflecting boundary is realized as a termination of the lattice at the edge position n_{edge} (yellow couplers) for every (b) even or (c) odd roundtrip m .

fiber and splits every roundtrip into two counterparts that are meanwhile detected by photoreceivers inserted in each of the loops [Fig. 1(a)]. Since the loop lengths are different, the resulting pulses become mutually delayed and thus detected at numerous discrete arrival times. There are two types of time delays between detected pulses. The first $T = \bar{L}/c \approx 20 \mu\text{s}$ is the average roundtrip time of the pulses where $c \approx 2 \times 10^8 \text{ m/s}$ is the speed of light in the fiber medium. The second $\Delta T = \Delta L/c \approx 200 \text{ ns}$ is associated with the loop length difference and defines a delay (lead) time of pulses in the longer (shorter) loop after one roundtrip. In what follows, we associate the average roundtrip times with a discrete time step m and the small temporal steps $\Delta T/2$ with a discrete position n . In the case of the fastest possible spreading over the lattice, the number of available positions and time steps can be estimated as $n_{\text{max}} = 2\bar{L}/\Delta L \approx 200$ and $m_{\text{max}} = \bar{L}/\Delta L \approx 100$, respectively. Thus, we project the detected signals onto an artificial spatiotemporal lattice (Fig. 1). The group-velocity dispersion is negligible in the setup for the given propagation distances, meaning that each pulse can be solely characterized by a complex amplitude denoted with u_n^m and v_n^m for the short and the long loop, respectively. In order to vary the coupling ratio t/r between the loops (where t^2 denotes the fraction of the entering pulse energy remaining in the same loop and

r^2 that passing to the other loop, i.e., $t^2 + r^2 = 1$), we use an optical voltage-driven variable coupler with a typical rise and fall time of 250 ns and a maximum repetition rate of 100 kHz. Further, both loops incorporate identical dispersion-compensating fibers (DCFs), which allow the pulses to accumulate Kerr nonlinear phase shifts $\kappa|u_n^m|^2$ and $\kappa|v_n^m|^2$ over one roundtrip, where κ is an effective nonlinear coefficient of the DCFs. Unavoidable signal losses including those due to detection are effectively compensated by erbium-doped fiber amplifiers (EDFAs) inserted in each loop, thus restoring a quasisconservative setting. In conclusion, the iterative evolution of the pulse complex amplitudes are described by

$$u_n^{m+1} = (t_{n+1}^m u_{n+1}^m + i r_{n+1}^m v_{n+1}^m) e^{i\kappa(|t_{n+1}^m u_{n+1}^m|^2 + |r_{n+1}^m v_{n+1}^m|^2)}, \quad (1)$$

$$v_n^{m+1} = (t_{n-1}^m v_{n-1}^m + i r_{n-1}^m u_{n-1}^m) e^{i\kappa(|t_{n-1}^m v_{n-1}^m|^2 + |r_{n-1}^m u_{n-1}^m|^2)}, \quad (2)$$

where $t_n^m = \cos(\varphi_n^m)$ and $r_n^m = \sin(\varphi_n^m)$ are the trigonometrically defined dynamical coupling coefficients of the variable coupler.

III. LINEAR FLOQUET-BLOCH WAVES

As a parametric degree of freedom required for realizing the Floquet-like analog of the SSH model and related topological effects, we deliberately vary the coupling ratio t/r between the loops by using two values for φ_n^m for subsequent roundtrips as follows:

$$\varphi_n^m = \begin{cases} \varphi_o, & m = 1, 3, 5, \dots \\ \varphi_e, & m = 2, 4, 6, \dots \end{cases} \quad (3)$$

where φ_o and φ_e stand for odd and even time steps, respectively.

First, we analyze the linear or low-power dynamics of our system. Figures 2(a) and 2(b) show numerical simulations as well as experimental measurements of discrete diffraction dynamics following a local on-site excitation.

In order to describe the bulk properties of the system, it is instructive to derive the dispersion relation of plane waves in the form $|\Psi_n^m\rangle \equiv (u_k, v_k) e^{iE_m + ikn}$. Since the system is periodic in the longitudinal and transverse direction with the period $\Delta m = 2$ and $\Delta n = 2$, the eigenvalues and arguments of the Floquet-Bloch modes are restricted to $-\pi/2 < E \leq \pi/2$ and $-\pi/2 < k \leq \pi/2$, respectively. Substituting this ansatz into the linear version ($\kappa = 0$) of Eqs. (1) and (2) and solving a standard eigenvalue problem with respect to E gives rise to the following dispersion relation:

$$E_{\pm}(k) = \pm \frac{\arccos(\cos \varphi_o \cos \varphi_e \cos 2k - \sin \varphi_o \sin \varphi_e)}{2}. \quad (4)$$

Two dispersion branches $E_{\pm}(k)$, given by Eq. (4), represent the bulk properties of the linear Floquet-Bloch waves within the Brillouin zone (BZ), whereas gaps ΔE_0 and $\Delta E_{\pi/2}$ form around the frequencies $E = 0$ and $E = \pm\pi/2$, respectively [see Fig. 2(c)]. For some set of the coupling parameters, the gaps vanish and, as a consequence, the topological phase changes abruptly. Straightforward arithmetic calculations based on Eq. (4) yield conditions for the gap closing, summarized in Fig. 2(d). More specifically, the gap at $E = 0$ vanishes provided that either the condition $\varphi_o + \varphi_e = \pi p$ or $\varphi_o - \varphi_e = \pi/2 + \pi p$ is satisfied, where p is an integer. Also,

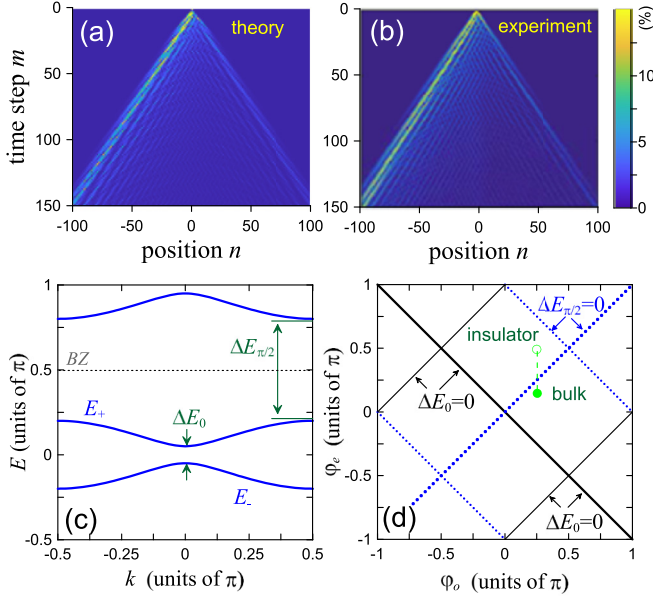


FIG. 2. (a) Theory and (b) experimental measurements of evolution dynamics of linear waves for a homogenous system with $\phi_o = 0.25\pi$ and $\phi_e = 0.13\pi$. (c) Dispersion relation of the bulk modes [see Eq. (4)] calculated for the parameters $\phi_o = 0.25\pi$ and $\phi_e = -0.35\pi$. The dashed horizontal line shows the boundary of the first Brillouin zone (BZ). Two independent band gaps for E_0 and $E_{\pi/2}$ form. (d) Phase diagram showing the closing of gaps on the parameter plane ϕ_o and ϕ_e . The black thick (thin) lines represent the closing of the gap E_0 for $k = 0$ ($k = 0.5\pi$). The dotted thick (thin) lines represent the closing of the gap $E_{\pi/2}$ for $k = 0.5\pi$ ($k = 0$). The vertical dashed line shows an example of the topological transition taking place for the trivial insulator, terminating the nontrivial bulk (the green disk at $\phi_e < \pi/4$) at even time steps (the green circle at $\phi_e = \pi/2$).

the gap at $E = \pm\pi/2$ closes for $\phi_o - \phi_e = \pi p$ or $\phi_o + \phi_e = \pi/2 + \pi p$. Due to the aforementioned bulk-boundary correspondence, gap-closing conditions, along with the dispersive properties of the bulk, predefine its topological properties, as will be discussed further below.

IV. TOPOLOGICALLY PROTECTED EDGE STATES (LINEAR REGIME)

Here we investigate the situation displayed in Fig. 1(b) and concentrate on the “edge,” i.e., a single-position isolating boundary between the lattice of interest, where light propagation is possible, and an “insulator” where by definition no light can propagate at least in a certain frequency range. One straightforward way to realize the insulator and hence the edge itself is to terminate a homogeneous lattice for $n \geq n_{\text{edge}}$, where n_{edge} is the edge position. The termination means setting the variable coupler to $t/r = 0/1$, so that the light entering the coupler from the long (short) loop gets reflected to the short (long) loop. Thus, inside the insulator, light permanently alternates between the loops, but cannot spread and thus remains trapped. Owing to such absence of transverse transport, we beforehand assign the insulator as topologically trivial.

In this regard and in accordance with the “bulk-boundary” theorem [26], the terminated bulk can be considered as topologically nontrivial if and only if there is a topologically protected state that locally resides on the lattice edge. In particular, the existence of the edge state is due to a topological transition at the boundary between the trivial and the nontrivial phase, which mathematically manifests itself as an abrupt change of an associated topological invariant, the so-called Zak phase or, its equivalent, the winding number. A rather common observation is that when continuously deforming the band structure of the trivial insulator to the nontrivial bulk (or vice versa) by smoothly tuning the coupling parameters, the topological transition and the abrupt change take place whenever one of the frequency gaps closes. In this context, the choice of the insulator for the trivial phase is not unique as will become clear from further considerations.

Despite our *a posteriori* definition of the topologically trivial or nontrivial phase, it has to be mentioned, however, that unlike in the canonical SSH lattice, where zero Zak phase (or winding number) is associated with the trivial phase, in the periodically driven lattice no such unambiguous connection can be made. And even if standard calculations yield zero Zak phase, the Floquet system may still exhibit topological edge states and they can appear even in pairs [14,22,39] (for a modified calculation of the topological invariant that correctly delivers the number of edge states for periodically driven systems in general and for our system in particular, please refer to [27] and to Appendices A–C).

Here, however, we avoid the need to explicitly evaluate the modified topological invariant and thus refer to another simpler method [40], which correctly predicts the number of present edge states and which has already been implemented for discrete quantum walks in [14,22]. First, we select two points in the coupling parameter space representing the bulk phase and the insulator phase. Here, for the bulk phase on the left side of the edge, we choose $\phi_o = \pi/4$, with ϕ_e being a free parameter, while the insulator on the right has the parameters $\phi_e = \pi/2$ or $\phi_o = \pi/2$ for the lattice termination at even [Fig. 1(b)] or odd [Fig. 1(c)] time steps, respectively. The other free parameter of the insulator (i.e., ϕ_o or ϕ_e) can, in principle, be chosen arbitrarily, but we fix it to the same value as for the bulk to simplify the experiment. Then, we connect the two points via a continuous path, which in the simplest case is a straight line, as illustrated in Fig. 2(d) for a termination of the lattice at even time steps. Finally, we count the parity of the number of times both gaps in the first BZ close to obtain the invariants Q_0 and $Q_{\pi/2}$ for the gaps $E = 0$ and $E = \pi/2$, respectively. If the lattice is terminated at even time steps, the invariant Q_0 is equal to 1 at $-0.75\pi < \phi_e < -0.25\pi$, corresponding to one existent edge state having frequency $E = 0$. Simultaneously, the protected mode of frequency $E = \pi/2$ is expected within the two parameter intervals $-\pi < \phi_e < 0.25\pi$ and $0.75\pi < \phi_e < \pi$. On the other hand, when the lattice is terminated at odd time steps, we get $Q_0 = 1$ ($Q_{\pi/2} = 1$) at $-0.75\pi < \phi_e < -0.25\pi$ ($0.25\pi < \phi_e < 0.75\pi$) predicting one edge state at $E = 0$ ($E = \pi/2$).

To verify these results, we calculated numerically the eigenmodes of the model in the linear limit, for varying system parameter ϕ_e [see Figs. 3(a) and 3(b)]. Among the

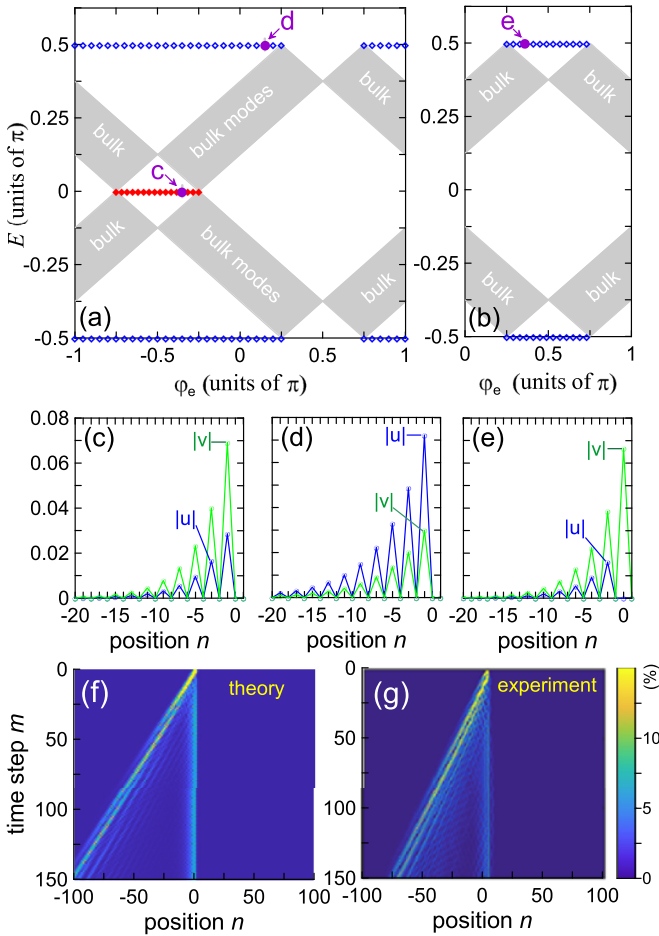


FIG. 3. (a),(b) Calculated eigenfrequencies of the linear extended (gray area) and the topological localized (blue and red dots) modes, where the bulk is set to $\varphi_o = \pi/4$ and terminated by the insulator for (a) even steps with $\varphi_e = \pi/2$ or (b) odd steps with $\varphi_o = \pi/2$. (c)–(e) Spatial profiles of the edge states (shown at odd m steps) calculated for $\varphi_e = -0.35\pi$, $\varphi_e = 0.15\pi$, and $\varphi_e = 0.35\pi$ as indicated in (a) and (b). (f) Numerical and (g) experimental on-site excitation of the topological edge state in the lattice with $\varphi_o = 0.25\pi$ and $\varphi_e = 0.185\pi$ and terminated at even time steps.

extended bulk modes, the localized edge modes occur in a full agreement with the method discussed above. Figures 3(c)–3(e) show the respective amplitude profiles of the stationary localized edge modes. As seen, most of the power at a fixed time step is concentrated mainly in one of their two components (u or v). This anisotropy is an indication of chirality of the state. Another feature, which is common with the edge states of the canonical SSH model [26], is an exponential decay of the amplitude distribution into the bulk with a characteristic localization length $\xi \sim 1/|\ln |t|/|r||$, where t and r are associated with hopping parameters of the original SSH chain.

In the experiment, the edge state can be excited with a relatively high coupling efficiency by a single pulse injection into one loop at the edge position n_{edge} , as shown in Figs. 3(f) and 3(g). In general, the coupling efficiency depends on the localization length of the edge state as the input signal has a form of δ distribution and thus does not have a perfect overlap

with the state. The rest of the energy is distributed between the bulk propagating waves. Finally, it is worth mentioning that the only experimentally accessible parametric region is $t, r \in (0, 1)$ since the relative phase between the complex transmission elements of the variable coupler does not depend on the operating voltage and is fixed. Thus, we assume, in the experiment, $0 < \varphi_{o,e} < 0.5\pi$, implying that the only gap at $E = \pi/2$ can close and thus the only edge state having $E = \pi/2$ can be observed there.

V. NONLINEAR TOPOLOGICAL EDGE STATES

In general, chiral symmetry of the system (see Appendix D for details) makes the topological edge states immune against perturbations and disorders that respect that symmetry. However, some local perturbations, while leaving the continuum of bulk states unaffected, as for instance the action of Kerr nonlinearity induced by a local field enhancement, are able to break chiral symmetry and thus cancel the effect of symmetry protection for a topological edge state. Nevertheless, the symmetry breaking does not necessarily affect the general existence of the edge state as soon as the nonlinear power level is not too high. In what follows, we will analyze steady-state edge states in the nonlinear case and check their stability against small perturbations.

Figure 4(a) shows a steady-state nonlinear solution, branching from the linear edge state at $E = -\pi/2$, calculated self-consistently with the corresponding nonlinear frequency shift. In the weak-intensity limit [Fig. 4(b)], the spatial profile is bounded and coincides with the linear edge state. The Kerr nonlinearity induces a positive phase shift, resulting in a nonlinear shift of the mode frequency E_{ed} . The spatial extension of the edge modes becomes wider for growing amplitude since the frequency of the edge modes shifts towards the linear band of the extended bulk modes (see, also, Appendix E). Furthermore, the edge mode delocalizes completely once its nonlinear frequency reaches the linear band edge ($E_{ed} = -0.425\pi$) [see Fig. 4(c)]. For that frequency, the mode becomes resonant to the continuum of the bulk and its excitation requires an infinite amount of energy.

To check whether the existing nonlinear steady-state edge modes are also protected and thus can persist infinitely long in the lattice, we perform a linear stability analysis of the steady-state profiles $|\Psi_n^{st}|$ against small perturbations. Thus, we are looking for solutions of the form $|\Psi_n^{(m)}\rangle = (|\Psi_n^{st}\rangle + |a_n\rangle e^{i\Omega m} + |b_n\rangle e^{-i\Omega m}) e^{iE_{ed}m}$, with $|a_n\rangle$ and $|b_n\rangle$ being small-amplitude perturbations. A standard linearization of the original model (1), (2), with respect to the small amplitudes $|a_n\rangle$ and $|b_n\rangle$, gives rise to an eigenvalue problem for the frequencies Ω of the perturbations. In addition to newly arising bound states, it contains the bulk spectrum of the original linear system and its replica mirrored on the frequency of the nonlinear solution [see Fig. 4(e)].

A steady-state solution becomes unstable provided that a small perturbation grows exponentially with time steps m , i.e., the imaginary part of any (at least one) linear mode becomes different from zero, $\text{Im}\Omega \neq 0$ [dashed lines in Fig. 4(a)]. The growth rate of the unstable mode is a monotonously growing function of the nonlinear frequency (E_{ed}) for frequencies higher than $E_{ed} \approx -0.477\pi$, which we refer to further as a

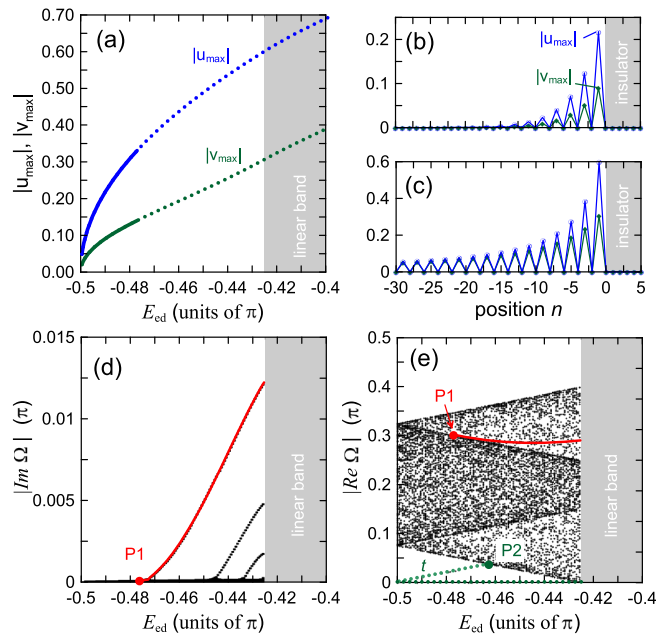


FIG. 4. (a) Maximum amplitudes $|u_{\max}|$ and $|v_{\max}|$ of the steady-state edge modes with the eigenfrequency E_{ed} calculated for nonlinear systems ($\kappa \neq 0$). Dashed lines depict unstable solutions. (b),(c) The amplitude profiles of edge modes in two regimes: (b) weak-power limit for $E_{ed} = -0.49\pi$ and (c) strongly nonlinear regime in the vicinity of the linear band edge for $E_{ed} = -0.425\pi$. (d) The result of linear stability analysis showing the growth rates of unstable modes ($|\text{Im}\Omega|$) vs the eigenfrequency of the steady-state solution (E_{ed}). The bifurcation point of the localized linear mode with maximum growth rate is depicted by “P1” ($E_{ed} = -0.477\pi$). (e) The real part of eigenvalues ($\text{Re}\Omega$) vs E_{ed} . The dots show spatially extended linear (bulk) modes. The red solid line depicts the localized mode with maximum growth rate. The linearized spectrum also contains a topological edge mode (“ t ”) depicted by the green dotted line. It crosses the extended modes in the point “P2” ($E_{P2} = -0.462\pi$). Other parameters are $\varphi_o = 0.25\pi$, $\varphi_e = 0.10\pi$, and $\kappa = 1$.

destabilization threshold of the nonlinear edge state (“P1”), as shown in Fig. 4(d). It is worth noting that the nonlinear edge mode becomes unstable much before its growing frequency reaches the linear band (given by $E_{ed} \approx -0.425\pi$). In Appendix E, we dynamically probe steady-state solutions below and above the destabilization threshold “P1” and thereby confirm results of the numerical stability analysis.

The leading unstable mode of the nonlinear edge mode is spatially localized around the edge, even though it bifurcates from an infinitely extended bulk mode within the continuous spectrum, represented in Fig. 4(e). In addition to this unstable linear mode, there are other spatially confined modes. The first one is associated with the phase symmetry of the steady-state solution and has zero eigenvalue ($\Omega = 0$, called “Goldstone” mode). Another one is associated with the reappearance of the linear topologically protected edge state [marked by “ t ” in Fig. 4(e)]. The frequency of this topological mode stays constant (note that we have split the nonlinear mode frequency, which causes a linear increase with E_{ed}). Although this mode reaches the bulk spectrum of the linearized problem for $E_{ed} = E_{P2} = -0.462\pi$, we do not see

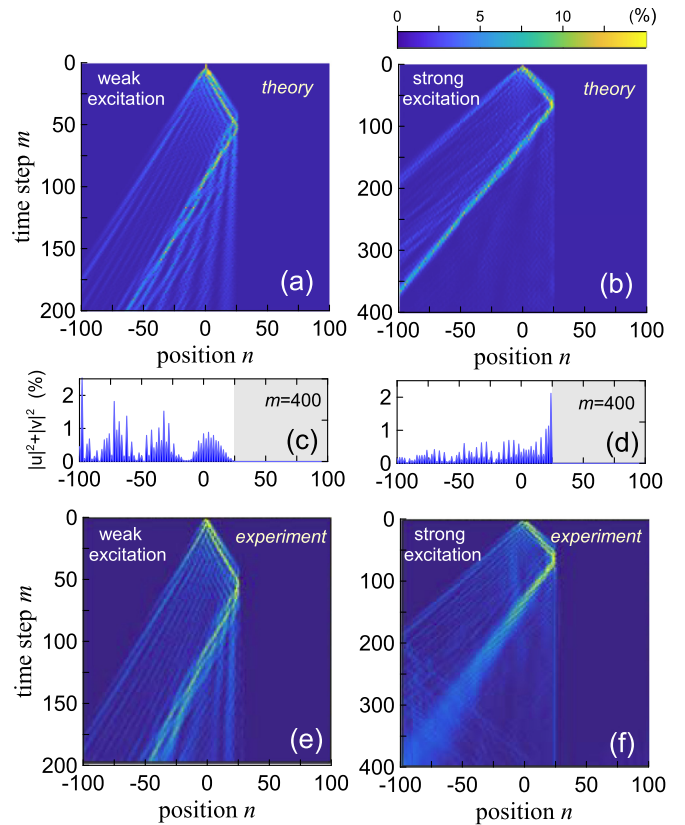


FIG. 5. Nonlinear excitation of the edge mode by a propagating pump pulse ($\varphi_o = 0.25\pi$, $\varphi_e = 0.3\pi$, the termination at odd time steps and at the position $n_{\text{edge}} = 24$, the pulse excitation at $n = 0$). (a) and (e) Evolution of the total energy ($|u_n^m|^2 + |v_n^m|^2$) in the weak-amplitude (linear) limit. (b),(f) Remote excitation of the edge mode in the nonlinear regime. (c),(d) Power distributions after $m = 400$ time steps for the weak- and strong-excitation regimes, presented in (a) and (b), respectively. The energy is normalized to the input energy of the seeding pulse.

any indication of mode mixing. For even stronger nonlinearity ($E_{ed} > -0.425\pi$), the gap in the spectrum closes and, as discussed above, the nonlinear edge state delocalizes.

Due to the stability transition of the edge mode, the energy being carried by the edge mode is limited. A further increase of input energy only causes a growth of unstable bulk mode and an emission of excess energy until the topologically protected edge state recovers again (see, also, Appendix E). The instability, discussed above, demonstrates the nonlinear interaction of the nontrivial edge state with extended bulk modes, a process which can also be used for pumping the edge states. As will be shown below, a direct excitation of the edge state by nonlinear waves is indeed possible.

VI. NONLINEAR PUMPING OF THE EDGE STATES

If we launch an input signal at a substantial distance from the edge site n_{edge} , so that the spatial overlap of the input signal with the edge mode vanishes, an excitation becomes impossible in the weak-power (linear) limit. We demonstrate this both numerically and experimentally in Figs. 5(a) and 5(e), respectively. However, the situation changes drastically

for a strong enough amplitude of the input signal, for which the nonlinearity is not negligible. If the input pulse is injected into the longer loop v only, a beam is formed that propagates towards the edge. It is worth mentioning that this nonlinear wave packet can propagate over a long distance without considerably changing its shape, sharing properties of gap solitons found in the continuum limit [41]. Once the nonlinear wave reaches the edge, a considerable energy transfer to the edge state takes place [see Figs. 5(b) and 5(d)]. Even though the nonlinear wave gets reflected backwards and travels away, a part of its energy becomes trapped within the edge state [compare the linear and nonlinear regimes shown in Figs. 5(c) and 5(d)].

For the given excitation scheme, the amount of trapped light does not exceed 6% and 3% in the lattice terminated at odd and even time steps, respectively. This relatively low transfer efficiency is mainly due to the demanding phase-matching condition, which has to be satisfied for both quasimomenta and frequencies. Also a certain optimization of the initial field distribution with regard to these requirements could noticeably increase the transfer efficiency. Nevertheless, the nonlinear pumping has been experimentally realized even with the δ -like initial distribution, as shown in Figs. 5(b) and 5(f). Due to a gradually increasing level of phase decoherence in the experimental setup [38], the nonlinear waves get dissolved after around 150 time steps, as it becomes evident from the comparison with the numerical simulation. On the other hand, once excited, the edge state is able to coherently trap the light for more than 400 time steps.

VII. CONCLUSIONS

The nonlinear dynamics of topologically protected edge modes in the 1D Floquet-Bloch photonic lattice has been studied both theoretically and experimentally. It has been proven that localized edge states exist in the presence of Kerr nonlinearity unless its nonlinearly shifted frequency overcomes the forbidden gap for linear modes. But even before, they become unstable against small perturbations, resulting in radiation of excess energy into the bulk. A remote excitation of the edge state by nonlinear waves has been demonstrated as well.

ACKNOWLEDGMENTS

This work was supported by the International Research Training Group 2101 ‘‘Guided light, tightly packed: novel concepts, components and applications.’’ Furthermore, it was supported by the Deutsche Forschungsgemeinschaft (DFG Project No. PE 523/18-1) and (DFG Project No. PE 523/14-1).

APPENDIX A: EFFECTIVE HAMILTONIANS OF THE FLOQUET-BLOCH WAVES

In this Appendix, we derive two equivalent effective bulk Hamiltonians of the Floquet system and the associated dispersion relation [see Eq. (4)]. In order to find the effective Hamiltonian of the model, we shall derive the stroboscopic evolution operator, promoting a state over two time steps

(temporal period of the modulated lattice) forward. We will see later that because of the temporal (Floquet) periodicity of the lattice, the evolution operator can be defined in two mutually shifted time frames, which eventually lead to two different Hamiltonians with distinct topological properties.

So, let us consider an arbitrary state of the quasiparticle walking on the (1 + 1)-dimensional lattice at some particular time step m ,

$$|\psi\rangle^m = \sum_{n=-\infty}^{+\infty} |n\rangle \otimes (u_n^m |u\rangle + v_n^m |v\rangle), \quad (\text{A1})$$

where Dirac quantum notations are used, u_n^m and v_n^m are complex probability amplitudes of the state, $|n\rangle$ are position eigenstates of the quasiparticle, and the eigenstates $|u\rangle$ and $|v\rangle$ represent the internal degree of freedom, associated with the short and the long loop of the setup, respectively, and often referred to as a pseudospin or coin state of the quasiparticle. The normalization condition for the wave function reads $\sum_n (|u_n|^2 + |v_n|^2) = 1$.

Since the evolution period contains two consecutive time steps and thus the stroboscopically promoted state can be alternatively chosen at even or odd time steps, we can write the evolution operator in two mutually shifted time frames, namely,

$$\hat{U}_{oe} = \widehat{S}\widehat{C}(\varphi_e)\widehat{S}\widehat{C}(\varphi_o), \quad (\text{A2})$$

$$\hat{U}_{eo} = \widehat{S}\widehat{C}(\varphi_o)\widehat{S}\widehat{C}(\varphi_e), \quad (\text{A3})$$

where

$$\widehat{C}(\varphi) \equiv \sum_{n=-\infty}^{\infty} |n\rangle\langle n| \otimes \begin{pmatrix} \cos(\varphi) & i \sin(\varphi) \\ i \sin(\varphi) & \cos(\varphi) \end{pmatrix}, \quad (\text{A4})$$

$$\widehat{S} \equiv \sum_{n=-\infty}^{\infty} \begin{pmatrix} |n+1\rangle\langle n| & 0 \\ 0 & |n-1\rangle\langle n| \end{pmatrix} \quad (\text{A5})$$

are the so-called coin and shift operators, locally mixing pseudospin components and shifting them to adjacent positions, respectively. The 2×2 matrices are acting locally on pseudospins, which have to be represented in the vector form $(u_n^m, v_n^m)^T$. Note that those evolution operators are equivalent to the iterative equations (1) and (2) introduced in the main text for the Floquet model. Later on, without loss of generality, we fix φ_o to $\pi/4$ (50/50 splitting ratio of the beam splitter), while letting φ_e be arbitrary. Note that any state on the lattice always occupies only odd positions (sublattice A) at odd time steps and even ones (sublattice B) at even time steps, as follows from Figs. 1(b) and 1(c) of the main text. Also, the two evolution operators describe wave dynamics in the same infinite bulk, but in different time frames.

Now, according to Bloch theorem, any state in the periodic lattice can be represented in terms of Bloch waves,

$$|k\rangle = \begin{pmatrix} u(k) \\ v(k) \end{pmatrix} \sum_n e^{-ink} |n\rangle, \quad (\text{A6})$$

where the pseudospin components are periodic functions of the quasimomentum k and the discrete position n runs over odd or even positions, depending on which evolution operator

is chosen. In this Fourier basis, the shift operator reads

$$\widehat{S} = \frac{1}{\pi} \int_{-\pi/2}^{\pi/2} dk \begin{pmatrix} e^{ik} & 0 \\ 0 & e^{-ik} \end{pmatrix} \otimes |k\rangle\langle k|, \quad (\text{A7})$$

while the coin operator, acting homogeneously and locally on the pseudospins, essentially remains the same:

$$\widehat{C}(\varphi) \equiv \frac{1}{\pi} \int_{-\pi/2}^{\pi/2} |k\rangle\langle k| dk \otimes \begin{pmatrix} \cos(\varphi) & i \sin(\varphi) \\ i \sin(\varphi) & \cos(\varphi) \end{pmatrix}. \quad (\text{A8})$$

The integral runs over the first Brillouin zone, which is reduced to $2\pi/N = \pi$ due to the spatial period of the lattice $N = 2$. Note that the shift operator became diagonal in the reciprocal basis. Thus, the evolution operators should also have the diagonal form $\widehat{U} = \frac{1}{\pi} \int \widehat{U}(k) |k\rangle\langle k| dk$, with

$$\begin{aligned} \widehat{U}_{oe,eo}(k) &= \begin{pmatrix} e^{ik} & 0 \\ 0 & e^{-ik} \end{pmatrix} \begin{pmatrix} \cos \varphi_{e,o} & i \sin \varphi_{e,o} \\ i \sin \varphi_{e,o} & \cos \varphi_{e,o} \end{pmatrix} \\ &\times \begin{pmatrix} e^{ik} & 0 \\ 0 & e^{-ik} \end{pmatrix} \begin{pmatrix} \cos \varphi_{o,e} & i \sin \varphi_{o,e} \\ i \sin \varphi_{o,e} & \cos \varphi_{o,e} \end{pmatrix}, \quad (\text{A9}) \end{aligned}$$

where φ_o is fixed to $\pi/4$. In other words, the momentum-dependent matrix amplitude $\widehat{U}(k)$ is acting in the internal space on each individual Bloch wave as $\psi^{m+2}(k) = \widehat{U}(k)\psi^m(k)$, where the time step m is either odd or even, depending on which evolution operator is chosen. Therefore, we can further diagonalize the operator in the internal space by solving the standard eigenvalue problem $\widehat{U}(k)\psi^m(k) = e^{i2E(k)}\psi^m(k)$, where $E(k)$ is the eigenspectrum of quasienergies and the factor 2 indicates the doubled temporal period of the evolution. It is not surprising that both evolution operators yield the same band structure since the wave dynamics in both cases has to be the same, as mentioned above. Indeed, the band structure for both evolution operators reads

$$E_{\pm}(k) = \pm \frac{1}{2} \arccos \left[\frac{\cos(2k) \cos(\varphi_e) - \sin(\varphi_e)}{\sqrt{2}} \right], \quad (\text{A10})$$

where the positively defined energy band has its symmetric negatively defined counterpart due to the so-called chiral (sublattice) symmetry, considered further below. As a result of this symmetry, two eigenmode solutions (one for each band) mutually exchange their respective eigenenergies when the evolution operator is switched from one type to another. This switch essentially flips the sublattice A with odd positions into the sublattice B with even positions, and vice versa.

To conclude this section, we derive the effective Hamiltonian of the system. It is clear now that since the hopping rates (coupling strengths) between one and another sublattice are not reciprocal in the Floquet system (unless $\varphi_o = \varphi_e$), the system loses time-reversal symmetry on the ‘‘microscopic’’ level of a single time step. On the other hand, the stroboscopic effective description with the doubled period respects time-reversal symmetry, though at the cost of the ambiguity in the choice of the evolution operator. It is clear that the effective Floquet Hamiltonian is subject to the same ambiguity. Indeed, writing the evolution matrix in terms of identity matrix \hat{I} and celebrated Pauli matrices $\vec{\sigma} \equiv (\hat{\sigma}_x, \hat{\sigma}_y, \hat{\sigma}_z)$ as $\widehat{U} =$

$\widehat{I} \cos 2E + i(\vec{a} \cdot \vec{\sigma}) \sin 2E$ and using the generalized Euler’s formula $\widehat{U} = \exp[2iE(\vec{a} \cdot \vec{\sigma})]$, we find the Hamiltonians as

$$\widehat{H}_{oe,eo}(k) = |E_{\pm}(k)| \vec{a}_{oe,eo}(k) \cdot \vec{\sigma}, \quad (\text{A11})$$

$$\begin{aligned} \vec{a}_{oe}(k) &= \frac{(\cos \varphi_e \cos 2k + \sin \varphi_e, -\cos \varphi_e \sin 2k, \cos \varphi_e \sin 2k)}{\sqrt{2} \sin |2E_{\pm}(k)|}, \quad (\text{A12}) \end{aligned}$$

$$\begin{aligned} \vec{a}_{eo}(k) &= \frac{(\cos \varphi_e + \cos 2k \sin \varphi_e, -\cos \varphi_e \sin 2k, \cos \varphi_e \sin 2k)}{\sqrt{2} \sin |2E_{\pm}(k)|}, \quad (\text{A13}) \end{aligned}$$

where $\vec{a}(k)$ is a three-dimensional real-valued unit vector, representing eigenmodes of the corresponding Hamiltonian on the so-called Bloch or Poincaré sphere. As an example, we illustrate $a_{oe}(k)$ for a fixed φ_e below $\pi/4$, while k sweeps over the first Brillouin zone.

APPENDIX B: TOPOLOGICAL INVARIANT OF THE EFFECTIVE FLOQUET HAMILTONIANS

According to the classification of topological insulators [23], the effective Floquet Hamiltonians respecting chiral (sublattice) and time-reversal symmetries fall into the same category as the canonical SSH model, namely, into the chiral orthogonal class BDI. Hence, each of the two Floquet Hamiltonians can be characterized by the topological invariant \mathbb{Z} , which is the winding number of the associated real-valued vector $\vec{a}(k)$ around the origin of the Bloch sphere. All in all, the full Floquet system with two gaps is characterized by the composed topological invariant $\mathbb{Z} \times \mathbb{Z}$, according to the extended classification of Floquet systems [42,43].

Next, due to chiral symmetry of our system, which will be demonstrated in the next section of the Appendix, the vector $\vec{a}(k)$ always lies in a tilted plane crossing the origin of the Bloch sphere, as shown in Fig. 6. Therefore, one can always align this plane in parallel to, for example, the xy plane and write the winding number of $\vec{a}(k) = a_x(k)\vec{e}_x + a_y(k)\vec{e}_y$ around the z axis as

$$W(\varphi_e) \equiv \frac{1}{\pi} \int_{-\pi/2}^{\pi/2} \left(a_x \frac{\partial a_y}{\partial k} - a_y \frac{\partial a_x}{\partial k} \right) dk, \quad (\text{B1})$$

where the integration is taken over the first Brillouin zone. The winding number is directly connected to another topological invariant called the Zak phase via $Z = -\pi W$. Rigorous calculation of the integral yields

$$W_{oe,\pm}(\varphi_e) = \begin{cases} 1, & \varphi_e \in (-\pi, -\frac{3\pi}{4}) \cup (-\frac{\pi}{4}, \frac{\pi}{4}) \cup (\frac{3\pi}{4}, \pi) \\ 0 & \text{otherwise,} \end{cases} \quad (\text{B2})$$

$$W_{eo,\pm}(\varphi_e) = \begin{cases} 1, & \varphi_e \in (\frac{\pi}{4}, \frac{3\pi}{4}) \\ -1, & \varphi_e \in (-\frac{3\pi}{4}, -\frac{\pi}{4}) \\ 0 & \text{otherwise.} \end{cases} \quad (\text{B3})$$

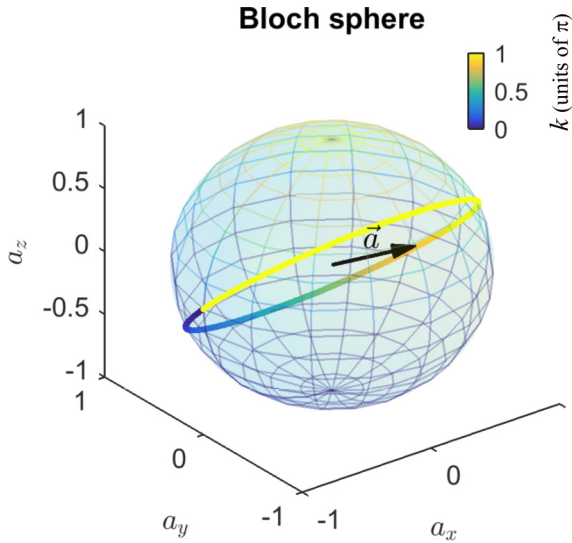


FIG. 6. Visualization of eigenmodes with the three-dimensional vector $a_{oe}(k)$ on the Bloch sphere at $\varphi_e < \pi/4$.

As seen, the Hamiltonian in the first time frame reveals one topologically nontrivial [$W_{oe,\pm}(\varphi_e) = 1$] and one topologically trivial [$W_{oe,\pm}(\varphi_e) = 0$] phase, while the second Hamiltonian along with the topologically trivial phase has in addition two different topologically nontrivial ones [$W_{eo,\pm}(\varphi_e) = \pm 1$]. Plots of the winding numbers are provided below in Fig. 7. Note that wherever the first Hamiltonian is topologically trivial (nontrivial), the second one is nontrivial (trivial). One can explicitly check that the points of the topological phase transitions correspond to a closing of the band gap at $E = 0$ or $E = \pi/2$. However, the obtained winding numbers do not provide enough information in order to correctly predict the existence of topological edge states (bulk-edge correspon-

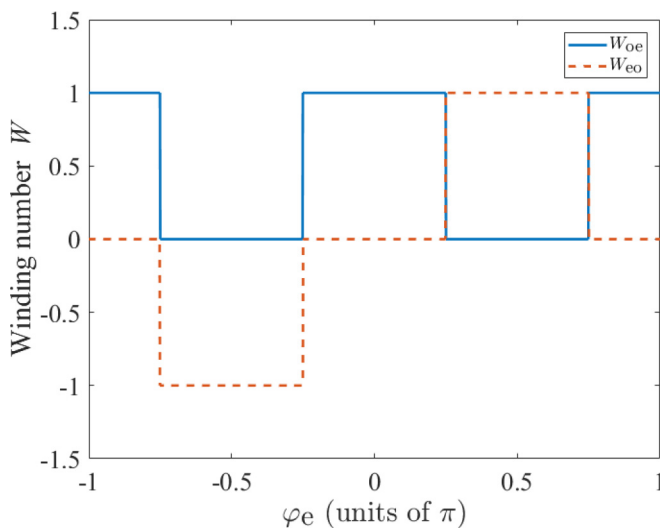


FIG. 7. Zero (nonzero) winding number indicates the trivial (nontrivial) topological phase of the associated Hamiltonian. An abrupt change of the winding numbers manifests a topological transition and closing of one of the two band gaps.

dence). Therefore, one has to input some additional information, as will be argued in Appendix C.

APPENDIX C: BULK-EDGE CORRESPONDENCE AND EDGE STATES IN THE FLOQUET SYSTEM

Although, in the main text, we give an easy graphical method to estimate the number of topological edge states [see Fig. 2(d)], here we establish an explicit connection between the topological invariants and the number of edge states in each gap for each termination type.

In the canonical SSH model, a topological edge state spectrally occurs in the middle of the zero-energy band gap, only if the topological phase of the SSH Hamiltonian is nontrivial. However, the Floquet system under consideration has two gaps (at $E = 0$ and $E = \pi/2$) and two topologically different effective Hamiltonians. A number of studies show that even if the topological invariant is zero, Floquet systems still may exhibit topological edge states. This circumstance is nonetheless explored more in two-dimensional models [44–47]. This is also the case in our system, where the topologically trivial phase of $\hat{H}_{oe}(k)$ within the parametric region $\varphi_e \in (-0.75\pi, -0.25\pi)$ indeed supports a pair of edge states, as illustrated in Fig. 8 above. Therefore, the found winding numbers are not directly related to the number of edge states, appearing in one or another gap. A straightforward solution to this problem is based on the so-called chiral symmetry time frames, which are demonstrated in [27,28,48] and in Appendix D on chiral symmetry. However, the bulk-edge correspondence relations can be partly deduced from the previously obtained winding numbers as well, if one considers the following semiheuristic argumentations.

Let us consider the spatiotemporal lattice depicted in Figs. 1(b) and 1(c), where the termination takes place at one position at odd and even time steps, respectively. Thus, the termination of the lattice is possible only at the sublattice A with odd or the sublattice B with even positions, but not at both of them simultaneously. Accordingly, the pseudospin

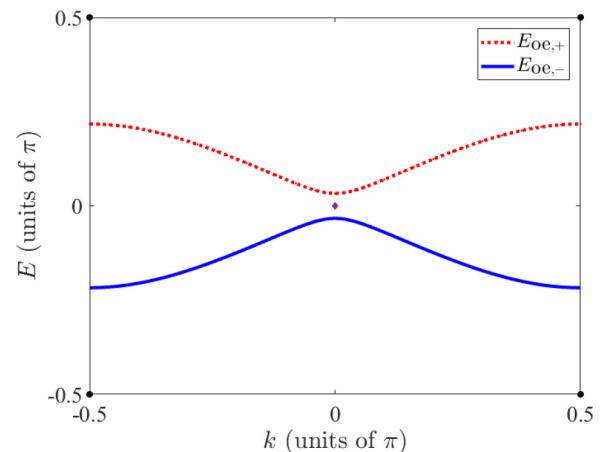


FIG. 8. The band structure, which is numerically calculated for the lattice terminated at even time steps, corresponding to the sublattice B. The terminated lattice supports two topological edge states, one at $E = 0$ and another at $E = \pi/2$, if $\varphi_e \in (-0.75\pi, -0.25\pi)$, $\varphi_o = -0.32\pi$.

located at the termination position of a particular sublattice splits componentwise between the bulk and the insulator regions. In other words, an abstract state occupying the terminated sublattice in the bulk region should necessarily contain that one pseudospin component belonging to the insulator. Therefore, the bulk evolution operator which stroboscopically promotes such a state should also formally promote that pseudospin component in the insulator. But this component, even though physically unoccupied, is coupled to the rest of the insulator. Thus, in this time frame, the evolution of the terminated bulk cannot be described in a closed form since the insulator region has to be included as well into the description. Therefore, one is forced to choose another operator, namely, \hat{U}_{oe} (\hat{U}_{eo}), if the termination takes place at sublattice B (A). It implies that the lattice termination physically resolves the ambiguity of the Floquet evolution operator. Therefore, in accordance with the bulk-edge correspondence principle, the topological winding number (W_{oe} or W_{eo}) of the associated bulk Hamiltonian dictates the existence conditions only for the edge states of the appropriately terminated lattice (sublattice B or A). Keeping this in mind and recalling that a pair of edge states can appear in the trivial phase as well, we can write

$$N_{A,\pi/2} - N_{A,0} = W_{eo}(\varphi_e), \quad (C1)$$

$$N_{B,\pi/2} - N_{B,0} = W_{oe}(\varphi_e),$$

or

$$N_{A,\pi/2} - N_{A,0} = -W_{eo}(\varphi_e), \quad (C2)$$

$$N_{B,\pi/2} - N_{B,0} = -W_{oe}(\varphi_e),$$

where $N_{i,\epsilon}$ is the number of edge states with the quasienergy $E = \epsilon$, provided the termination is at sublattice i . These relations have the form of the Index theorem [17,49–51] and, due to a lack of information, they have that sign ambiguity. Rigorous calculation of the band structures of the terminated bulk shows that relations on the left-hand side are the right ones. Another ambiguity is that in the trivial phases, either zero or two edge states can appear, one in each gap. As already mentioned above, a pair of edge states appears only if the bulk, being described by \hat{H}_{oe} with $\varphi_e \in (-0.75\pi, -0.25\pi)$, is terminated at even time steps (sublattice B).

In conclusion, the winding numbers found in these particular time frames allow only for a partial reconstruction of the bulk-edge correspondence. As already mentioned, the exact relations can be found if one considers the chiral symmetric time frames. In Appendix D, we will, however, use them for another purpose, namely, to demonstrate chiral symmetry of the lattice.

APPENDIX D: CHIRAL (SUBLATTICE) SYMMETRY OF THE FLOQUET SYSTEM

This Appendix is devoted to chiral symmetry, which is responsible for symmetry protection of the topological edge states [52]. We explicitly show that chiral symmetry holds for the linear lattice, including the special case of a terminated lattice, but argue that Kerr nonlinearity should necessarily destroy the symmetry, thereby canceling the effect of symmetry protection.

It is known that the middle-gap edge mode of the canonical one-dimensional SSH chain is protected by the so-called chiral or sublattice symmetry of the lattice against disorders that do not destroy this symmetry [52]. The same protection mechanism holds for chiral edge states of Floquet discrete time quantum walks (DTQWs) because, according to Ref. [28] (see left column on page 2), “a DTQW has chiral symmetry, if there is a time frame where its effective Hamiltonian has chiral symmetry.” In what follows, we will show that given the chiral symmetry operator is fixed, two such time frames exist for our particular system in the linear regime. Moreover, since the chiral symmetry operator itself is defined ambiguously, the pair of time frames, where the effective Hamiltonians are chiral, can be different as well.

First of all, the chiral symmetry operator is by definition a unitary operator $\hat{\Gamma}_n$, acting locally on a pseudospin situated in the position n . Thus, for the entire lattice, it can be defined either homogeneously or not. We define it homogeneously as

$$\sum_n \hat{\Gamma}_n \otimes |n\rangle\langle n| = \hat{\Gamma} \otimes \sum_n |n\rangle\langle n|, \quad (D1)$$

$$\hat{\Gamma} \equiv \hat{\sigma}_y, \quad (D2)$$

where the choice of the Pauli matrix $\hat{\sigma}_y$ is not unique, but is predefined by the time frame, which we are going to choose later on. A Hamiltonian is said to obey the chiral symmetry if $\hat{\Gamma}\hat{H}\hat{\Gamma}^{-1} = -\hat{H}$ or, equivalently, $\hat{\Gamma}\hat{U}\hat{\Gamma}^{-1} = \hat{U}^{-1}$. In order to show that this chiral symmetry is preserved for the terminated lattice, we will consider the even more generalized case, where the coin operators are inhomogeneously defined, namely,

$$\hat{U} = \sum_n \hat{S}_n \hat{C}(\varphi_{e,n}) \hat{S}_n \hat{C}(\varphi_{o,n}), \quad (D3)$$

where n runs over odd or even positions, depending on the time frame chosen. Let us transform the evolution operator into the previously mentioned chiral symmetry time frame, which has been widely used in Floquet periodic systems [27,28,48]. The new time frame is obtained by the following cyclic permutation:

$$\hat{U}_{\text{sym}} = \sum_n \hat{C}\left(\frac{\varphi_{o,n}}{2}\right) \hat{S}_n \hat{C}(\varphi_{e,n}) \hat{S}_n \hat{C}\left(\frac{\varphi_{o,n}}{2}\right), \quad (D4)$$

where the factorization property $\hat{C}(\varphi_{o,n}/2)\hat{C}(\varphi_{o,n}/2) = \hat{C}(\varphi_{o,n})$ of the coin operator has been used. Note that another time frame, where the operator $\hat{C}(\varphi_{o,n})$ is placed in the center, can be chosen as well. Now, we can explicitly derive that

$$\begin{aligned} \hat{\Gamma} \hat{U}_{\text{sym}} \hat{\Gamma}^{-1} &= \hat{\Gamma} \left[\sum_n \hat{C}\left(\frac{\varphi_{o,n}}{2}\right) \hat{S}_n \hat{C}(\varphi_{e,n}) \hat{S}_n \hat{C}\left(\frac{\varphi_{o,n}}{2}\right) \right] \hat{\Gamma}^{-1} \\ &= \sum_n \hat{\Gamma} \hat{C}\left(\frac{\varphi_{o,n}}{2}\right) \hat{\Gamma}^{-1} \hat{\Gamma} \hat{S}_n \hat{\Gamma}^{-1} \\ &\quad \times \hat{\Gamma} \hat{C}(\varphi_{e,n}) \hat{\Gamma}^{-1} \hat{\Gamma} \hat{S}_n \hat{\Gamma}^{-1} \hat{\Gamma} \hat{C}\left(\frac{\varphi_{o,n}}{2}\right) \hat{\Gamma}^{-1}, \end{aligned} \quad (D5)$$

$$\begin{aligned} \hat{U}_{\text{sym}}^{-1} &= \sum_n \left[\hat{C}\left(\frac{\varphi_{o,n}}{2}\right) \hat{S}_n \hat{C}(\varphi_{e,n}) \hat{S}_n \hat{C}\left(\frac{\varphi_{o,n}}{2}\right) \right]^{-1} \\ &= \sum_n \hat{C}^{-1}\left(\frac{\varphi_{o,n}}{2}\right) \hat{S}_n^{-1} \hat{C}^{-1}(\varphi_{e,n}) \hat{S}_n^{-1} \hat{C}^{-1}\left(\frac{\varphi_{o,n}}{2}\right). \end{aligned} \quad (D6)$$

It is easy to show that the equality $\hat{\Gamma}\hat{U}\hat{\Gamma}^{-1} = \hat{U}^{-1}$ holds if $\hat{\Gamma} = \hat{\sigma}_y$, provided that

$$\hat{\Gamma}\hat{C}\left(\frac{\varphi_{o,n}}{2}\right)\hat{\Gamma}^{-1} = \hat{C}^{-1}\left(\frac{\varphi_{o,n}}{2}\right), \quad (\text{D7})$$

$$\hat{\Gamma}\hat{C}(\varphi_{e,n})\hat{\Gamma}^{-1} = \hat{C}^{-1}(\varphi_{e,n}), \quad (\text{D8})$$

$$\hat{\Gamma}\hat{S}_n\hat{\Gamma}^{-1} = \hat{S}_n^{-1}, \quad \forall n. \quad (\text{D9})$$

Therefore, the uniformly defined chiral symmetry holds even for the lattice with an inhomogeneously defined coin operator, including the terminated one with the edge; hence, the chiral symmetry protection of the topological edge states.

In conclusion, we show that the Kerr nonlinearity breaks the uniformly defined chiral symmetry $\hat{\Gamma}$ of the lattice, by considering the nonlinear propagator:

$$\hat{U}_{\text{sym}}^{2m} = \sum_n \hat{C}\left(\frac{\varphi_{o,n}}{2}\right)\hat{K}_n^{2m+1}\hat{S}_n\hat{C}(\varphi_{e,n})\hat{K}_n^{2m}\hat{S}_n\hat{C}\left(\frac{\varphi_{o,n}}{2}\right), \quad (\text{D10})$$

$$\hat{K}_n^m \equiv \begin{pmatrix} e^{i\kappa|u_n^m|^2} & 0 \\ 0 & e^{i\kappa|v_n^m|^2} \end{pmatrix}, \quad (\text{D11})$$

where the operators \hat{K}_n^m are locally defined and associated with the intensity-dependent self-phase modulation, and one evolution step covers two time steps in accordance with the Floquet SSH-like model. Taking time reversal of the nonlinear propagator implies that along with the transformations in Eq. (D1), the nonlinear operators \hat{K}_n^{2m} and \hat{K}_n^{2m+1} should permute and the Kerr coefficient should change its sign, $\kappa \rightarrow -\kappa$. Thus, we come up with

$$\begin{aligned} \hat{U}_{\text{sym}}^{-1} &= \sum_n \left[\hat{C}\left(\frac{\varphi_{o,n}}{2}\right)\hat{K}_n^{2m+1}\hat{S}_n\hat{C}(\varphi_{e,n})\hat{K}_n^{2m}\hat{S}_n\hat{C}\left(\frac{\varphi_{o,n}}{2}\right) \right]^{-1} \\ &= \sum_n \hat{C}^{-1}\left(\frac{\varphi_{o,n}}{2}\right)(\hat{K}_n^{2m})^{-1}\hat{S}_n^{-1} \\ &\quad \times \hat{C}^{-1}(\varphi_{e,n})(\hat{K}_n^{2m+1})^{-1}\hat{S}_n^{-1}\hat{C}^{-1}\left(\frac{\varphi_{o,n}}{2}\right). \end{aligned} \quad (\text{D12})$$

By applying $\hat{\Gamma}\hat{U}\hat{\Gamma}^{-1} = \hat{U}^{-1}$, we get, in addition to relations (29)–(31), the following conditions:

$$\Gamma\hat{K}_n^{2m+1}\Gamma^{-1} = (\hat{K}_n^{2m})^{-1}, \quad (\text{D13})$$

$$\Gamma\hat{K}_n^{2m}\Gamma^{-1} = (\hat{K}_n^{2m+1})^{-1}. \quad (\text{D14})$$

Obviously, in the presence of nonlinear perturbations, these conditions cannot be satisfied with $\hat{\Gamma} = \hat{\sigma}_y$ simultaneously for all positions n . Therefore, the uniformly defined chiral symmetry is broken and, consequently, the symmetry protection [52], ensuring the spectral isolation of the topological edge states from extended bulk modes has to be lifted. Nevertheless, the topological edge states are able to survive and propagate stably up to a moderate nonlinearity level, as we demonstrate in our work. This indicates that the symmetry protection can be lifted without destroying the topological edge state.

APPENDIX E: VERIFIED STABILITY OF THE NONLINEAR TOPOLOGICAL EDGE STATE

In this Appendix, we retrieve the nonlinear steady-state solutions and verify their stability by means of a direct nu-

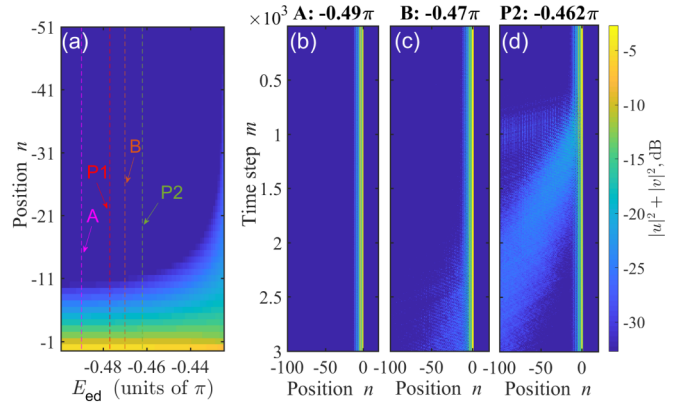


FIG. 9. (a) Normalized intensity profiles (logarithmic scale) of the nonlinear steady-state solutions vs eigenfrequencies E_{ed} . (b)–(d) Evolution dynamics of the nonlinear edge states launched with a uniformly distributed random noise of approximately 1% of the maximal intensity. (b) Stable propagation for $E_{ed} = -0.49\pi$, depicted by vertical dashed line “A” in (a). (c) Unstable propagation for $E_{ed} = -0.47\pi$ (depicted by “B”). (d) Strongly unstable dynamics for $E_{ed} = -0.462\pi$ (depicted by “P2”). Other parameters are similar to those in Fig. 4.

merical simulation within the frame of the original model (1), (2). Figure 9(a) shows normalized total intensity profiles of the nonlinear steady states versus its eigenfrequency (E_{ed}). As already mentioned in Sec. V, spatial extension of the edge modes becomes broader for increasing values of E_{ed} and diverges in the vicinity of the upper band of extended linear modes.

Now, we probe the results of the linear stability analysis, given in Fig. 4(d), by launching some of those steady-state solutions with an additional small-amplitude noise into the evolution equations (1) and (2). In doing so, we consider first the nonlinear solution at point “A,” where the state is supposed to be stable. Indeed, the state propagates stably without any noticeable growth of the initial random noise or any energy loss by the edge state [see Fig. 9(b)]. Further, we pick up a solution “B” [see Fig. 9(c)] beyond the instability point “P1” and propagate it for the same number of time steps. As expected, the profile starts to experience growing perturbations, which become visible after approximately 2000 time steps. Finally, we increase the eigenfrequency even further [see Fig. 9(d)] and observe already after 500 time steps that the unstable edge mode radiates a substantial part of energy into the bulk modes. Thus, a large amount of light escapes the edge within a relatively short period of time, so that the remaining power gets trapped within a newly stabilized and almost completely linear edge state.

We performed further simulations (not shown here) of a single-pulse on-site excitation of a nonlinear edge state, similar to the linear case in Figs. 3(f) and 3(g). As expected, one can excite any nonlinear edge state up to the instability point “P1” by varying the amplitude of the input pulse. However, a substantial part of the energy immediately escapes the edge due to the spatial and momentum mismatch of the input field, discussed above in Sec. IV. The maximum amount of the trapped light energy, which was achieved in our simulations, was about 15% of the total energy.

- [1] C. L. Kane and E. J. Mele, Z_2 Topological Order and the Quantum Spin Hall Effect, *Phys. Rev. Lett.* **95**, 146802 (2005).
- [2] B. A. Bernevig, T. L. Hughes, and S.-C. Zhang, Quantum spin Hall effect and topological phase transition in HgTe quantum wells, *Science* **314**, 1757 (2006).
- [3] C. L. Kane and E. J. Mele, Quantum Spin Hall Effect in Graphene, *Phys. Rev. Lett.* **95**, 226801 (2005).
- [4] R. El-Ganainy and M. Levy, Optical isolation in topological-edge-state photonic arrays, *Opt. Lett.* **40**, 5275 (2015).
- [5] M. C. Rechtsman, J. M. Zeuner, Y. Plotnik, Y. Lumer, D. Podolsky, F. Dreisow, S. Nolte, M. Segev, and A. Szameit, Photonic Floquet topological insulators, *Nature (London)* **496**, 196 (2013).
- [6] Z. Wang, Y. Chong, J. D. Joannopoulos, and M. Soljacic, Observation of unidirectional backscattering-immune topological electromagnetic states, *Nature (London)* **461**, 772 (2009).
- [7] N. Malkova, I. Hromada, X. Wang, G. Bryant, and Z. Chen, Observation of optical Shockley-like surface states, *Opt. Lett.* **34**, 1633 (2009).
- [8] A. B. Khanikaev, S. H. Mousavi, W.-K. Tse, M. Kargarian, A. H. MacDonald, and G. Shvets, Photonic topological insulators, *Nat. Mater.* **12**, 233 (2013).
- [9] M. Hafezi, S. Mittal, J. Fan, A. Migdall, and J. M. Taylor, Imaging topological edge states in silicon photonics, *Nat. Photon.* **7**, 1001 (2013).
- [10] M. Hafezi, E. A. Demler, M. D. Lukin, and J. M. Taylor, Robust optical delay lines with topological protection, *Nat. Phys.* **7**, 907 (2011).
- [11] M. Verbin, O. Zilberberg, Y. E. Kraus, Y. Lahini, and Y. Silberberg, Observation of Topological Phase Transitions in Photonic Quasicrystals, *Phys. Rev. Lett.* **110**, 076403 (2013).
- [12] M. Verbin, O. Zilberberg, Y. Lahini, Y. E. Kraus, and Y. Silberberg, Topological pumping over a photonic Fibonacci quasicrystal, *Phys. Rev. B* **91**, 064201 (2015).
- [13] Y. E. Kraus, Y. Lahini, Z. Ringel, M. Verbin, and O. Zilberberg, Topological States and Adiabatic Pumping in Quasicrystals, *Phys. Rev. Lett.* **109**, 106402 (2012).
- [14] T. Kitagawa, M. A. Broome, A. Fedrizzi, M. S. Rudner, E. Berg, I. Kassal, A. Aspuru-Guzik, E. Demler, and A. G. White, Observation of topologically protected bound states in photonic quantum walks, *Nat. Commun.* **3**, 882 (2012).
- [15] H. Schomerus, Topologically protected midgap states in complex photonic lattices, *Opt. Lett.* **38**, 1912 (2013).
- [16] T. E. Lee, Anomalous Edge State in a Non-Hermitian Lattice, *Phys. Rev. Lett.* **116**, 133903 (2016).
- [17] K. Esaki, M. Sato, K. Hasebe, and M. Kohmoto, Edge states and topological phases in non-Hermitian systems, *Phys. Rev. B* **84**, 205128 (2011).
- [18] G. Harari, M. A. Bandres, Y. Lumer, M. C. Rechtsman, Y. D. Chong, M. Khajavikhan, D. N. Christodoulides, and M. Segev, Topological insulator laser: Theory, *Science* **359**, eaar4003 (2018).
- [19] M. A. Bandres, S. Wittek, G. Harari, M. Parto, J. Ren, M. Segev, D. N. Christodoulides, and M. Khajavikhan, Topological insulator laser: Experiments, *Science* **359**, eaar4005 (2018).
- [20] P. St-Jean, V. Goblot, E. Galopin, A. Lemaître, T. Ozawa, L. Le Gratiet, I. Sagnes, J. Bloch, and A. Amo, Lasing in topological edge states of a one-dimensional lattice, *Nat. Photon.* **11**, 651 (2017).
- [21] S. Klemmt, T. H. Harder, O. A. Egorov, K. Winkler, R. Ge, M. A. Bandres, M. Emmerling, L. Worschech, T. C. Liew, M. Segev, C. Schneider, and S. Höfling, Exciton-polariton topological insulator, *Nature (London)* **562**, 552 (2018).
- [22] T. Kitagawa, M. S. Rudner, E. Berg, and E. Demler, Exploring topological phases with quantum walks, *Phys. Rev. A* **82**, 033429 (2010).
- [23] A. P. Schnyder, S. Ryu, A. Furusaki, and A. W. W. Ludwig, Classification of topological insulators and superconductors in three spatial dimensions, *Phys. Rev. B* **78**, 195125 (2008).
- [24] A. Kitaev, Periodic table for topological insulators and superconductors, in *Advances in Theoretical Physics: Landau Memorial Conference*, edited by V. Lebedev and M. Feigel'man, AIP Conf. Proc. 1134 (AIP, New York, 2009), p. 22.
- [25] W. P. Su, J. R. Schrieffer, and A. J. Heeger, Solitons in Polyacetylene, *Phys. Rev. Lett.* **42**, 1698 (1979).
- [26] J. K. Asbóth, L. Oroszlány, and A. Pályi, *A Short Course on Topological Insulators: Band Structure and Edge States in One and Two Dimensions* (Springer, Heidelberg, 2016).
- [27] J. K. Asbóth, B. Tarasinski, and P. Delplace, Chiral symmetry and bulk-boundary correspondence in periodically driven one-dimensional systems, *Phys. Rev. B* **90**, 125143 (2014).
- [28] J. K. Asbóth and H. Obuse, Bulk-boundary correspondence for chiral symmetric quantum walks, *Phys. Rev. B* **88**, 121406(R) (2013).
- [29] F. Grusdt, M. Höning, and M. Fleischhauer, Topological Edge States in the One-Dimensional Superlattice Bose-Hubbard Model, *Phys. Rev. Lett.* **110**, 260405 (2013).
- [30] S. Ryu and Y. Hatsugai, Zero-energy edge states and chiral symmetry breaking at edges of graphite sheets, *Physica E* **22**, 679 (2004).
- [31] D. A. Dobrykh, A. V. Yulin, A. P. Slobozhanyuk, A. N. Poddubny, and Yu. S. Kivshar, Nonlinear Control of Electromagnetic Topological Edge States, *Phys. Rev. Lett.* **121**, 163901 (2018).
- [32] S. Kruk, A. Poddubny, D. Smirnova, L. Wang, A. Slobozhanyuk, A. Shorokhov, I. Kravchenko, B. Luther-Davies, and Y. Kivshar, Nonlinear light generation in topological nanostructures, *Nat. Nanotechn.* **14**, 126 (2019).
- [33] D. D. Solnyshkov, O. Bleu, B. Teklu, and G. Malpuech, Chirality of Topological Gap Solitons in Bosonic Dimer Chains, *Phys. Rev. Lett.* **118**, 023901 (2017).
- [34] Y. Hadad, A. B. Khanikaev, and Andrea Alù, Self-induced topological transitions and edge states supported by nonlinear staggered potentials, *Phys. Rev. B* **93**, 155112 (2016).
- [35] A. Regensburger, C. Bersch, M.-A. Miri, G. Onishchukov, D. N. Christodoulides, and U. Peschel, Parity-time synthetic photonic lattices, *Nature (London)* **488**, 167 (2012).
- [36] M. Wimmer, H. M. Price, I. Carusotto, and U. Peschel, Experimental measurement of the Berry curvature from anomalous transport, *Nat. Phys.* **13**, 545 (2017).
- [37] A. Regensburger, M.-A. Miri, C. Bersch, J. Näger, G. Onishchukov, D. N. Christodoulides, and U. Peschel, Observation of Defect States in PT-Symmetric Optical Lattices, *Phys. Rev. Lett.* **110**, 223902 (2013).
- [38] M. Wimmer, A. Regensburger, M.-A. Miri, C. Bersch, D. N. Christodoulides, and U. Peschel, Observation of optical solitons in PT-symmetric lattices, *Nat. Commun.* **6**, 7782 (2015).

- [39] T. Kitagawa, Topological phenomena in quantum walks: Elementary introduction to the physics of topological phases, *Quantum Inf. Proc.* **11**, 1107 (2012).
- [40] J. K. Asbóth, Symmetries, topological phases, and bound states in the one-dimensional quantum walk, *Phys. Rev. B* **86**, 195414 (2012).
- [41] D. A. Smirnova, L. A. Smirnov, D. Leykam, and Y. S. Kivshar, Topological edge states and gap solitons in the nonlinear Dirac model, *Laser Photon. Rev.* **13**, 1900223 (2019).
- [42] R. Roy and F. Harper, Periodic table for Floquet topological insulators, *Phys. Rev. B* **96**, 155118 (2017).
- [43] F. Nathan and M. Rudner, Topological singularities and the general classification of Floquet-Bloch systems, *New J. Phys.* **17**, 125014 (2015).
- [44] M. S. Rudner, N. H. Lindner, E. Berg, and M. Levin, Anomalous Edge States and the Bulk-Edge Correspondence for Periodically Driven Two-Dimensional Systems, *Phys. Rev. X* **3**, 031005 (2013).
- [45] L. Maczewsky, J. Zeuner, S. Nolte, and A. Szameit, Observation of photonic anomalous Floquet topological insulators, *Nat. Commun.* **8**, 13756 (2017).
- [46] S. Mukherjee, A. Spracklen, M. Valiente, E. Andersson, P. Öhberg, N. Goldman, and R. Thomson, Experimental observation of anomalous topological edge modes in a slowly driven photonic lattice, *Nat. Commun.* **8**, 13918 (2017).
- [47] D. Leykam, M. C. Rechtsman, and Y. D. Chong, Anomalous Topological Phases and Unpaired Dirac Cones in Photonic Floquet Topological Insulators, *Phys. Rev. Lett.* **117**, 013902 (2016).
- [48] D. Kim, M. Ken, N. Kawakami, and H. Obuse, Floquet Topological Phases Driven by PT Symmetric Nonunitary Time Evolution, [arXiv:1609.09650](https://arxiv.org/abs/1609.09650).
- [49] M. Sato, Y. Tanaka, K. Yada, and T. Yokoyama, Topology of Andreev bound states with flat dispersion, *Phys. Rev. B* **83**, 224511 (2011).
- [50] M. Kremer, *Topological Effects in Fibre Networks* (Masterarbeit, Friedrich-Schiller-Universität Jena, 2017).
- [51] T. Morimoto and N. Nagaosa, Topological nature of nonlinear optical effects in solids, *Sci. Adv.* **2**, e1501524 (2016).
- [52] M. Franz and L. Molenkamp, *Topological Insulators*, Vol. 6 (Elsevier, New York, 2013).